Mass transport in the cathode of a free-breathing polymer electrolyte membrane fuel cell

T. MENNOLA*, M. NOPONEN, M. ARONNIEMI, T. HOTTINEN, M. MIKKOLA, O. HIMANEN and
P. LUND
*Helsinki University of Technology, Laboratory of Advanced Energy Systems, Rakentajanaukio 2 C, FIN-02150,
Espoo, Finland*
(*author for correspondence, e-mail: tuomas.mennola@hut.fi)

Abstract

In small fuel cell applications, it is desirable to take care of the management of reactants, water and heat by passive means in order to minimize parasitic losses. A polymer electrolyte membrane fuel cell, in which air flow on the cathode was driven by free convection, was studied by experimental and modelling methods. The cathode side of the cell had straight vertical channels with their ends open to the ambient air. A two-dimensional, isothermal and steady state model was developed for the cathode side to identify the limiting processes of mass transport. The modelled domain consists of the cathode gas channel and the gas diffusion layer. Experimental data from current distribution measurements were used to provide boundary conditions for oxygen consumption and water production. The model results indicate that at the cell temperature of 40 °C the performance of the cell was limited by water removal. At the cell temperature of 60 °C, the current distribution was determined by the partial pressure of oxygen.

List of symbols

Variables and Constants

a	empirical constant
b	empirical constant
B	half-width of channel (m)
c	concentration (mol m^{-3})
D	diffusion coefficient (m^2 s^{-1})
E	voltage (V)
F	Faraday's constant (96 485 C mol^{-1})
g	acceleration due to gravity (9.81 m s^{-2})
H	width of model domain (m)
j	current density (mA cm^{-2})
L	channel length (m)
M	molecular mass (kg mol^{-1})
n	normal vector
N	flux of species (mol m^{-2} s^{-1})
p	pressure (atm or Pa)
R	universal gas constant (8.3514 J mol^{-1} K^{-1})
RH	relative humidity (%)
T	temperature (K or °C)
u	x-component of velocity (m s^{-1})
u	velocity (m s^{-1})
v	y-component of velocity (m s^{-1})
X	mole fraction
x	horizontal coordinate in the model (m)
y	vertical coordinate in the model (m)
z	coordinate perpendicular to xy-plane (m)

Subscripts

0	conditions at inlet
amb	ambient
ave	average
cell	fuel cell
cr	critical
eff	effective
gdl	gas diffusion layer
i	species
j	species
N	nitrogen
O	oxygen
sat	saturation
W	water

Greek letters

α	net water transport
ε	porosity
μ	dynamic viscosity (kg m^{-1} s^{-1})
ρ	density (kg m^{-3})
Σv	diffusion volume

1. Introduction

The rapid development of polymer electrolyte membrane fuel cells (PEMFCs) during the past decade has

brought practical applications close to reality. The largest part of research efforts has been devoted to the development of kW-scale applications, most notably fuel cell electric vehicles. Recently, there has also been increasing interest in small fuel cells that could be used as a replacement for batteries. Possible applications include portable electronic devices, such as laptop and palmtop computers and mobile phones [1–3], as well as small stationary applications such as self-sufficient solar hydrogen systems [4]. Military applications are also being developed [5–8]. PEMFCs or direct methanol fuel cells (DMFCs) are usually regarded as the most promising fuel cell types for small applications.

Compared to batteries, fuel cells potentially offer significant benefits, such as longer operating times and fast refueling. In addition, the environmental effect of discarded batteries is regarded as a problem. However, fuel cell technology is not yet mature enough to compete with established battery technologies in everyday consumer applications. To make fuel cells competitive with batteries, the fuel cell system needs to be miniaturized, and the complexity and power consumption of auxiliary components should be minimized. For example, external humidification and temperature control systems are undesirable. Effective air supply and water management must be ensured using methods that are as insensitive as possible to varying environmental conditions. In portable applications, the cell should also be insensitive to physical orientation.

In very small PEMFC stacks, free convection is an attractive method for air supply, because it eliminates the need for a compressor or fan to feed the reactant air into the cathode. However, when air supply cannot be directly controlled, the choice of the geometry and materials of the cell becomes very critical for achieving good and reliable performance.

Modelling studies can be used to gain insight into mass transport phenomena in a fuel cell and to obtain information about quantities that are difficult to measure directly. These include, for example, the gas flow velocity, and the local mole fractions of oxygen and water. Numerous modelling studies exist on mass transport in forced-convection cells. Important early works include the models of Bernardi and Verbrugge [9, 10], and Springer et al. [11, 12]. Pseudo two-dimensional models have been reported by Fuller and Newman [13], and Nguyen and White [14]. More recently, elaborate two-dimensional models have been developed by Gurau et al. [15], Um et al. [16] and Dannenberg et al. [17]. Two-phase modeling has been considered a central issue in several recent modeling studies. Two-phase models have been formulated by Wang et al. [18], Natarajan et al. [19], He et al. [20], Janssen [21], Berning et al. [22], Rowe et al. [23], Wöhr et al. [24], Shimpalee et al. [25] and Shimpalee [26]. Some of the reported modeling efforts also account for transient phenomena [16, 19].

However, the authors of the present study are not aware of any reported modeling work on free-convection PEMFCs. In this study, we investigate mass transport on the cathode of a free-convection cell using measured current distribution data to prescribe boundary conditions for oxygen and water fluxes. Our previous experiments have revealed that significant local variations of current density may exist in a free-convection cell [27,28]. The purpose of the study is to provide theoretical explanations for the measured current distributions and to indicate methods for the modeling of free-convection PEMFCs. The model was implemented using the FEMLAB® multiphysics program (COMSOL AB) running within the MATLAB® environment.

2. Methods

2.1. Experimental

The experimental data for this study were obtained using a current distribution measurement system, built in our laboratory [27]. The essential part of the system was a specially designed cathode side flow field plate. The cathode channel geometry consisted of parallel straight channels with their ends open to the outside air. The flow field plate was segmented, which made it possible to measure the current density as a function of position on the active area. Current was collected with 48 gold plated stainless steel pins, in contact with the gas diffusion layer, but insulated from each other by the plastic supporting structure of the plate. This made it possible to measure the current through each current collector pin individually.

The anode side flow field plate was made of graphite. The gas diffusion layers at both cell sides were of type GDL 10 BB under the trademark® SIGRACET of SGL Technologies GmbH. The MEA was PRIMEA® Series 5510 MEA from W.L. Gore & Associates, with platinum loading of 0.3 mg cm^{-2} per electrode. The anode flow field plate, the gas diffusion layers, and the electrodes were not segmented.

The measurements were performed using a Globe-Tech GT-100 fuel cell test station. The current distributions were recorded using auxiliary data logging systems. The temperature and the relative humidity of ambient air during the measurements were recorded using a Vaisala HMI41 relative humidity and temperature indicator with a HMP42 probe.

2.2. Modelling

2.2.1. Governing equations
The model was constructed in two dimensions. The model is steady state, isothermal, and single-phase. It describes the active region of a vertically oriented air channel and the gas diffusion layer. In addition to the active region, there are 15 mm long lead-in and lead-out regions in the channels of the measurement plate. These are not included in the model. The cathode electrode is taken into account as a boundary condition. The model geometry is illustrated in Figure 1.
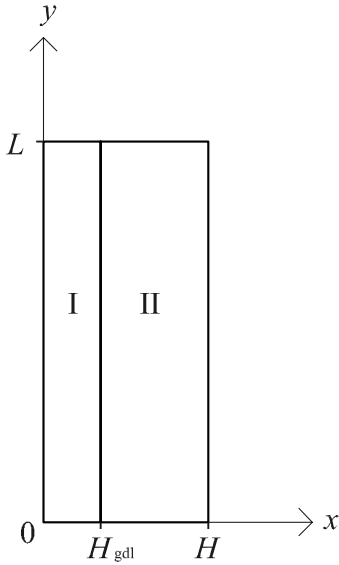
Fig. 1. Modelled domain, which consists of the gas diffusion layer (I) and the gas channel (II).

The steady-state continuity equation for mass is

$$\nabla \cdot \rho \mathbf{u} = 0 \tag{1}$$

The Navier–Stokes equation in its steady-state form is used to describe the velocity field in the channel region:

$$\rho \mathbf{u} \cdot \nabla \mathbf{u} = \mu \nabla^2 \mathbf{u} - \nabla p + \mathbf{g}(\rho - \rho_0) \tag{2}$$

To take the three-dimensional geometry of the channel into account, Poiseuille flow profile is used to describe the dependency of u and v on the z-coordinate:

$$u = \frac{3}{2}\left(1 - \frac{z^2}{B^2}\right)\langle u \rangle \tag{3a}$$

$$v = \frac{3}{2}\left(1 - \frac{z^2}{B^2}\right)\langle v \rangle \tag{3b}$$

where $\langle u \rangle$ and $\langle v \rangle$ are the averages of u and v over the z-coordinate. Navier–Stokes equation is integrated with respect to z-coordinate from the axis of symmetry to the wall, assuming Poiseuille flow profile. The x- and y-components of the resulting equation are:

$$\frac{6\rho}{5}\left(\frac{\partial\langle u\rangle^2}{\partial x} + \frac{\partial\langle u\rangle\langle v\rangle}{\partial y}\right)$$
$$= \mu\left(\frac{\partial^2\langle u\rangle}{\partial x^2} + \frac{\partial^2\langle u\rangle}{\partial y^2}\right) - \nabla p - g(\rho - \rho_0) - \frac{\mu\langle u\rangle}{B^2/3} \tag{4a}$$

$$\frac{6\rho}{5}\left(\frac{\partial\langle u\rangle\langle v\rangle}{\partial x} + \frac{\partial\langle v\rangle^2}{\partial y}\right)$$
$$= \mu\left(\frac{\partial^2\langle v\rangle}{\partial x^2} + \frac{\partial^2\langle v\rangle}{\partial y^2}\right) - \nabla p - g(\rho - \rho_0) - \frac{\mu\langle v\rangle}{B^2/3} \tag{4b}$$

where B is the half-width of the channel. The modified equations feature an additional 'Darcy-type' term on the right-hand side and the factor 6/5 in the inertial term. Equations 4 have been derived previously by Roos et al. [29].

An unmodified 2D-model would underestimate the flow resistance, because in reality the channel is not infinite to the z-direction. In a model free-convection cell, flow rate cannot be prescribed as an input parameter. Therefore, it is important that the flow resistance of the channel is correctly determined.

Buoyancy is included in the Navier–Stokes equation as an external force term. Buoyancy is driven by density differences, which result from thermal expansion and changes in the gas composition. When density variations are small, the Boussinesq approximation can be used to model free convection. This approach has been used to model free convection in a vertical channel, for example by Lee [30]. However, in the present case the density variations caused by the electrochemical reactions make it desirable to use a more elaborate buoyancy model. Therefore, the gas density is computed from the equation:

$$\rho = c \sum_i X_i M_i \tag{5}$$

The total concentration is calculated from the ideal gas law:

$$c = \frac{p}{RT} \tag{6}$$

Pressure variations can be assumed to be small and, therefore, a constant value was used for pressure in all other equations than (4) in order to accelerate numerical convergence.

The continuity of molar fluxes of oxygen and water in both model regions is expressed as:

$$\nabla \cdot \mathbf{N}_i = 0 \tag{7}$$

In the gas channel, the molar flux of a chemical species is defined as

$$\mathbf{N}_i = -D_i \nabla X_i + X_i c \langle \mathbf{u} \rangle \tag{8}$$

The diffusion coefficients in Equation 8 are calculated using the formula based on the work of Fuller et al. [31]:

$$D_{ij} = 0.0101 \frac{T^{1.75}\left(\frac{1}{M_i} + \frac{1}{M_j}\right)^{1/2}}{p\left[(\Sigma v_i)^{1/3} + (\Sigma v_j)^{1/3}\right]^2} \tag{9}$$

where p is pressure (Pa), T is temperature (K), and M is molecular mass (g mol^{-1}). The value of the diffusion volume Σv is 16.6 for O_2, 20.1 for air, and 12.7 for H_2O. The formula gives the diffusion coefficients in units of m^2 s^{-1}. The molar fraction of nitrogen is calculated from the molar fractions of oxygen and water using the equation

$$X_N = 1 - X_O - X_w \qquad (10)$$

In our notation, the diffusion coefficients with the single subscripts O and W refer to the diffusion coefficients for oxygen in air, and water vapor in air, respectively.

In the porous gas diffusion layer, species transport is governed by the Stefan-Maxwell equation:

$$\nabla X_i = \sum_j \frac{1}{cD_{ij}}(X_i \mathbf{N}_j - X_j \mathbf{N}_i) \qquad (11)$$

where D_{ij} is the binary diffusion coefficient of the gas pair i–j. Nitrogen is inert and thus its flux is set to zero. Solving for $\mathbf{N}_O$ and $\mathbf{N}_W$ in Equation 11, we obtain:

$$\mathbf{N}_O = -c \frac{D_{OW} D_{NO}}{D_{NO} X_W + D_{NW} X_O + D_{OW} X_N}$$
$$\times \left(\frac{X_O D_{NW}}{X_N D_{OW}} (\nabla X_W + \nabla X_O) + \nabla X_O \right) \qquad (12)$$

$$\mathbf{N}_W = -c \frac{D_{OW} D_{NW}}{D_{NO} X_W + D_{NW} X_O + D_{OW} X_N}$$
$$\times \left(\frac{X_W D_{NO}}{X_N D_{OW}} (\nabla X_W + \nabla X_O) + \nabla X_W \right) \qquad (13)$$

The diffusion coefficients that describe the binary diffusion of species in the gas diffusion layer are be obtained using the Slattery–Bird correlation [32]:

$$D_{ij} = \frac{a \left(\frac{T}{T_{cr,i} T_{cr,j}} \right)^b (p_{cr,i} p_{cr,j})^{1/3} (T_{cr,i} T_{cr,j})^{5/12} \left(\frac{1}{M_i} + \frac{1}{M_j} \right)^{1/2}}{p} \qquad (14)$$

where $T_{cr,i}$ and $T_{cr,j}$ are the critical temperatures (K), $p_{c,i}$ and $p_{c,j}$ are the critical pressures (atm), and M_i and M_j are the molecular masses (g mol^{-1}) of the species i and j, respectively. The values of the empirical constants a and b depend on the gas pair. For nonpolar gas pairs $a = 2.745 \times 10^{-4}$ and $b = 1.823$, and for the binary diffusion of water vapor with a nonpolar gas $a = 3.640 \times 10^{-4}$ and $b = 2.334$. The equation gives the diffusion coefficients in units of cm^2 s^{-1}. In our model, constant values are used for T and p. Before inserting into Equations 12 and 13, the diffusion coefficients are modified using the Bruggeman correlation, to account for the effect of the porosity of the gas diffusion layer:

$$D_{eff} = (\varepsilon^{1.5}) D \qquad (15)$$

2.2.2. Boundary conditions

The boundary conditions at the ends of the gas channel ($H_{gdl} < x < H$) are defined as follows:

$$X_i|_{y=0} = X_{i,0}, \quad \left. \frac{\partial X_i}{\partial y} \right|_{y=L} = 0$$

$$\left. \frac{\partial \langle v \rangle}{\partial y} \right|_{y=0} = 0, \quad \left. \frac{\partial \langle v \rangle}{\partial y} \right|_{y=L} = 0$$

$$p|_{y=0} = 0, \quad p|_{y=L} = 0 \qquad (16)$$

A constant pressure is defined at $y=0$ and $y=L$, because the ends of the channels are open to the ambient air. According to the boundary conditions (16), pressure is defined as gauge pressure. The mole fraction of water vapour was calculated from the measured ambient temperature and relative humidity, using the relation

$$X_{W,0} = \frac{p_{sat}}{p_{amb}} \text{RH} \qquad (17)$$

The mole fraction of oxygen was adjusted to account for the water vapour in air:

$$X_{O,0} = X_{O,amb}(1 - X_{W,0}) \qquad (18)$$

where the subscript amb refers to the mole fraction in dry standard air. At the impermeable rear wall of the gas channel, the following boundary conditions are defined:

$$\left. \frac{\partial X_i}{\partial x} \right|_{x=H} = 0, \qquad \mathbf{n} \cdot \langle \mathbf{u} \rangle|_{x=H} = 0, \qquad \left. \frac{\partial p}{\partial x} \right|_{x=H} = 0 \qquad (19)$$

At the boundary of the channel and the gas diffusion layer, velocity is determined from the fluxes of the species across the boundary, and the derivative of pressure in x-direction is set to zero:

$$\langle u \rangle|_{x=H_{gdl}} = \frac{1}{\rho} \left(\frac{(1+2\alpha)M_W}{2} - \frac{M_O}{4} \right) \frac{\mathbf{n} \cdot \mathbf{j}}{F}$$

$$\langle v \rangle|_{x=H_{gdl}} = 0$$

$$\left. \frac{\partial p}{\partial x} \right|_{x=H_{gdl}} = 0 \qquad (20)$$

The measured current distribution at the electrode is used to determine the fluxes of the species in the boundary condition for velocity at the boundary of the channel and the gas diffusion layer. This can be considered a valid approximation, because of the large aspect ratio of the gas diffusion layer region.

A constant value was used for ρ in Equation 20. The value was calculated assuming 50% relative humidity and $x_O = 0.5 x_{O,0}$. By varying the value, it could be ascertained that the effect of assumptions on the gas composition had a negligible effect on the results.

In the gas diffusion layer region, boundary conditions are only needed for the molar fractions. At the ends of

the gas diffusion layer ($0 < x < H_{\text{gdl}}$) the boundary conditions are defined as

$$\left.\frac{\partial X_i}{\partial y}\right|_{y=0} = 0, \quad \left.\frac{\partial X_i}{\partial y}\right|_{y=L} = 0 \qquad (21)$$

At the boundary between the gas diffusion layer and the electrode, the molar fluxes of oxygen and water are defined as

$$\mathbf{n} \cdot \mathbf{N_O}|_{x=0} = -\frac{\mathbf{n} \cdot \mathbf{j}(y)}{4F}, \quad \mathbf{n} \cdot \mathbf{N_W}|_{x=0} = \frac{\mathbf{n} \cdot (1 + 2\alpha)\mathbf{j}(y)}{2F} \qquad (22)$$

A measured current distribution was used for $\mathbf{j}(y)$. Using the current distribution measurement system, the local current density was obtained at four locations along the length of each rib of the flow field plate. The readings were averaged in the horizontal direction over the 12 ribs.

To avoid numerical difficulties at the boundaries of the segments, a third-degree polynomial curve was fitted to the data in order to obtain a smoothly changing distribution. The fitting leads to a minor error, because the integral of the curve does not exactly match the average current. This was corrected by adjusting the constant term of the polynomial. The corrected polynomial fit was used as $\mathbf{j}(y)$ in the boundary conditions.

2.2.3. Parameters

The common parameters used in the calculations are summarized in Table 1. The parameters, which are temperature-dependent, are listed in Table 2. In addition to these parameters, the current distribution, and the temperature and relative humidity of ambient air are needed. They were obtained from the measurements described in the next sub-chapter. The diffusion coefficients in Table 2 were obtained using Equations 9 and 14.

Boundary conditions (20) and (22) contain the parameter α, which is the average number of water molecules transported across the membrane per proton.

Table 1. Common parameters

α	-0.25
ε	0.6
H_{gdl}/m	0.3×10^{-3}
H/m	3.3×10^{-3}
L/m	0.05
M_N/kg mol^{-1}	28×10^{-3}
M_O/kg mol^{-1}	32×10^{-3}
M_W/kg mol^{-1}	18×10^{-3}
$p_{\text{cr,N}}$/Pa	3.39×10^6
$p_{\text{cr,O}}$/Pa	5.04×10^6
$p_{\text{cr,w}}$/Pa	22.1×10^6
p_0/Pa	101 325
$T_{\text{c,N}}$/K	126.2
$T_{\text{c,O}}$/K	154.6
$T_{\text{c,w}}$/K	647.1

Table 2. Temperature-dependent parameters

	$T_{\text{cell}} = 40\ °C$	$T_{\text{cell}} = 60\ °C$
D_O/m^2 s^{-1}	2.15×10^{-5}	2.39×10^{-5}
D_W/m^2 s^{-1}	2.87×10^{-5}	3.34×10^{-5}
D_{NO}/m^2 s^{-1}	2.25×10^{-5}	2.52×10^{-5}
D_{NW}/m^2 s^{-1}	2.94×10^{-5}	3.39×10^{-5}
D_{OW}/m^2 s^{-1}	2.81×10^{-5}	3.25×10^{-5}
μ/Ns m^{-2}	19.160×10^{-6}	20.072×10^{-6}
P_{sat}/Pa	7381.4	19 932

When hydrogen is fed into the cell without humidification, the direction of net water transport cannot be from the anode to the cathode. From Equation 22 it can be seen, that if $\alpha = 0$, all of the product water from the cathode reaction exits through the cathode outlet. Respectively, if $\alpha = -0.5$, all of the product water exits through the anode outlet. In this study, the measurement of water fluxes was not attempted and, therefore, an intermediate value of $\alpha = -0.25$ was assumed. The theoretical prediction of α would require a whole-cell model.

In an operating fuel cell, the gas diffusion layer is compressed and probably flooded to some degree. The effective porosity and thickness, therefore, need to be assumed. The nominal thickness of the gas diffusion layer was 0.42 mm and the thickness of the gaskets was 0.25 mm. The porosity $\varepsilon = 0.6$ was obtained by assuming that the gas diffusion layer was compressed to an average thickness of 0.3 mm, and that only the volume of the pores in the material was reduced under compression.

3. Results

3.1. Experimental details

Measurements were performed at cell temperatures of 40 and 60 °C. The measured ambient temperature and relative humidity during the measurements were 28 °C and 46%, respectively. The density of ambient air was calculated from these readings using Equation 5. Current distributions were recorded at the average current density levels of 100 and 200 mA cm^{-2} at both temperature levels. In addition, a current distribution at an average of 300 mA cm^{-2} was recorded at 60 °C. At 40 °C, stable performance at 300 mA cm^{-2} could not be achieved, due to flooding problems. Because the ends of the cathode channels are open to the ambient air, flooding problems could easily be detected by visually observing the accumulation of water in the channel.

In of the other cases, it was also found that cell voltage exhibited a tendency to fall and to become increasingly unstable in sustained operation. This type of behavior was observed at the highest included current density level at both of the temperature levels. However, it was considered useful to obtain a large variety of current distributions measured under different operating
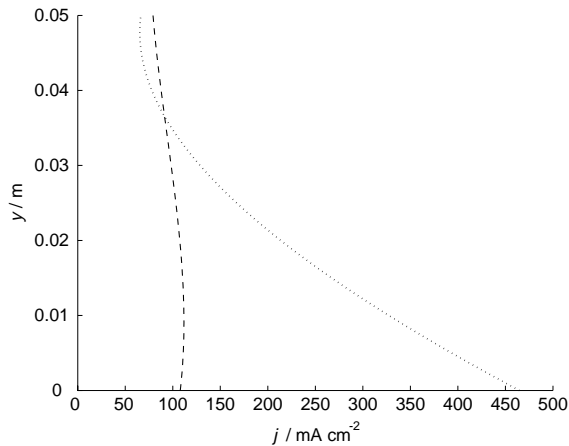
Fig. 2. Current distributions measured at T_{cell} = 40 °C. Key: (- - -) j_{ave} = 100 mA cm^{-2}; ($\cdots$) j_{ave} = 200 mA cm^{-2}.

conditions in order to gain a better insight into the limiting processes of mass transport. Therefore, these quasi-stable cases were also included in the data set and relatively short measurement times were used to achieve this. The recording of the current distributions was started after a stabilization period of 5 min and the distribution was measured as an average from a period of the following 5 min. The cell was operated in galvanostatic mode, which was found to result in relatively rapid stabilization of the current distribution readings, even when voltage was fluctuating.

The measured distributions are depicted in Figures 2 and 3. The cell voltages during the measurements are given in Table 3. The figures show that at the lowest average current density level the current distributions were relatively even. At higher average current densities, variations between the segments began to emerge. The highest current densities were always obtained at or near the lower end of the channel, and performance was found to decrease towards the upper end of the channel. This was especially notable in the 40 °C case. As seen in
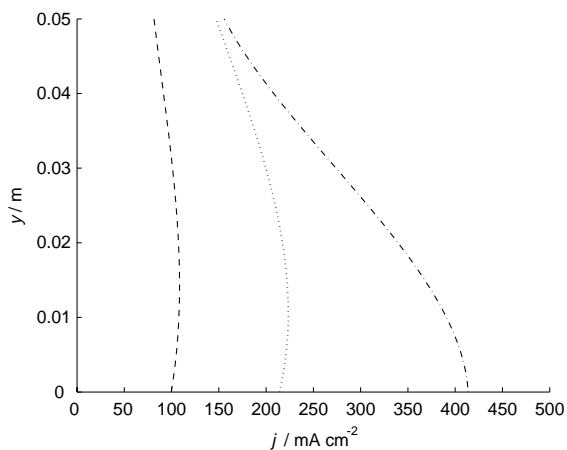

Fig. 3. Current distributions measured at T_{cell} = 60 °C. Key: (- - -) j_{ave} = 100 mA cm^{-2}; ($\cdots$) j_{ave} = 200 mA cm^{-2}; (------) j_{ave} = 300 mA cm^{-2}.

Table 3. Average cell voltages during current distribution measurements and root mean square deviation from the average

T_{cell}/°C	j_{ave}/mA cm^{-2}	E/V
40	100	0.703 ± 0.002
40	200	0.50 ± 0.07
60	100	0.748 ± 0.001
60	200	0.657 ± 0.002
60	300	0.55 ± 0.01

Table 3, the cell voltages exhibited a trend of increasing voltage fluctuations with increasing current density. When assessing the voltage stability, it should be remembered that due to the lack of control on the air supply, the level of short-term fluctuations of voltage in free-breathing cells is typically higher than in cells operating on forced convection.

Additional experiments were made with the cell in the horizontal orientation. It was found that performance suffered considerably compared to the vertically oriented case. Average current densities higher than 40 mA cm^{-2} could not be obtained. In addition, it was found that performance was not significantly improved with increasing temperature in this orientation. These observations indicate that diffusion alone is insufficient as a driving force of mass transport in this channel geometry. The orientation of the cell may have a slight effect on flooding, because droplets of liquid water cannot be removed from horizontally oriented channels by gravity. However, our experience shows that the removal of liquid water from the cell by gravity is relatively ineffective also in the vertically oriented case, and therefore, this factor is probably of minor importance.

3.2. Modelling

The model was solved to obtain the mole fractions of oxygen and water, and the velocity field. The model results for velocity are averaged in the z-direction, as explained in the description of the model. The results indicate that at the lower cell temperature water removal was the most significant limiting factor for cell performance, and at higher cell temperature the oxygen partial pressure limited the performance. Typical oxygen mole fraction profiles in the gas diffusion layer and the gas channel are shown in Figure 4. The mole fractions of water vapour in the channel and the gas diffusion layer are similarly depicted in Figure 5. The depicted case is T_{cell} = 60 °C and j_{ave} = 300 mA cm^{-2}. The rest of the model results are summarized in Tables 4 and 5.

Figures 4 and 5 show that the model predicts relatively small changes in the mole fractions to the x-direction within the gas diffusion layer. The oxygen mole fraction at the electrode surface appears to be primarily determined by the availability of oxygen in the channel. Similarly, the water mole fraction at the electrode follows closely the mole fraction profile in the channel region. However, it must be remembered that the diffusion path to the regions under the ribs of
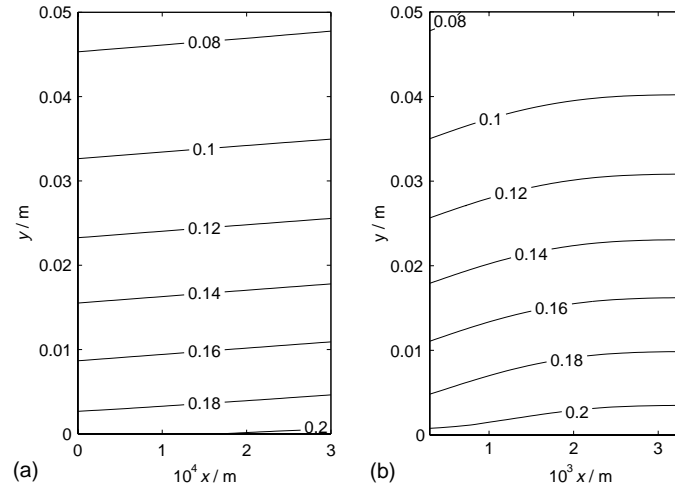
Fig. 4. Model results for the mole fraction of oxygen in the gas diffusion layer (a) and in the gas channel (b). $T_{cell} = 60\ °C$, $j_{ave} = 300\ mA\ cm^{-2}$.

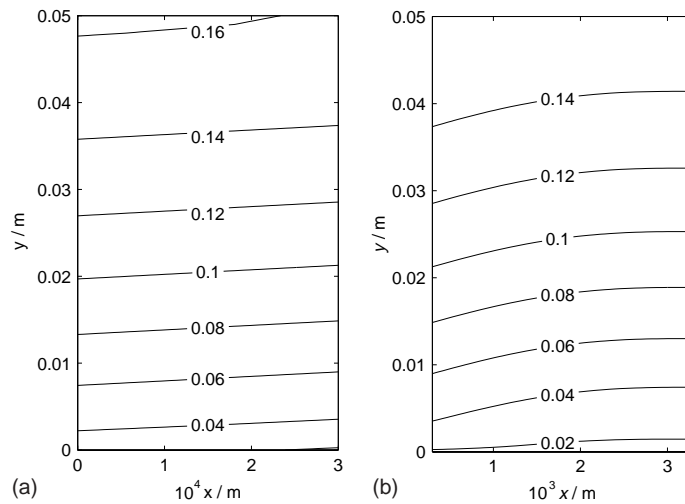
Fig. 5. Model results for the mole fraction of water vapour in the gas diffusion layer (a) and in the gas channel (b). $T_{cell} = 60\ °C$, $j_{ave} = 300\ mA\ cm^{-2}$.

Table 4. Model results for minimum oxygen mole fraction
Results are given in absolute figures and in percentage of mole fraction at inlet.

T_{cell} /°C	j_{ave} /mA cm^{-2}	Minimum of X_O	Minimum of X_O /$X_{O,0}$/%
40	100	0.127	61.6
40	200	0.0883	42.8
60	100	0.153	74.2
60	200	0.110	53.1
60	300	0.0757	36.7

Table 5. Model results for maximum water mole fraction and relative humidity

T_{cell} /°C	j_{ave} /mA cm^{-2}	Maximum of X_w	Maximum of RH /%
40	100	0.105	144
40	200	0.147	202
60	100	0.0758	38.6
60	200	0.124	63.0
60	300	0.162	82.2

the flow field is longer, and the model predictions therefore do not hold there. In addition, the porosity of the gas diffusion layer will be reduced if flooding takes place.

The profiles of oxygen and water mole fractions are strongly affected by the flow velocity. A typical velocity field in the channel region is depicted in Figure 6, and the velocities at the upper end of the channel are summarized in Table 6. The results shown in the Table are the magnitudes of the velocity vector at $y = L$, averaged in the x-direction from H_{gdl} to H. The average velocity at the end of the channel was less than $0.03\ m\ s^{-1}$ in all of the modelled cases. The effect of temperature is clearly seen in the results. The change in the gas composition also contributes to the velocity, because the gas density decreases towards the upper end of the channel.
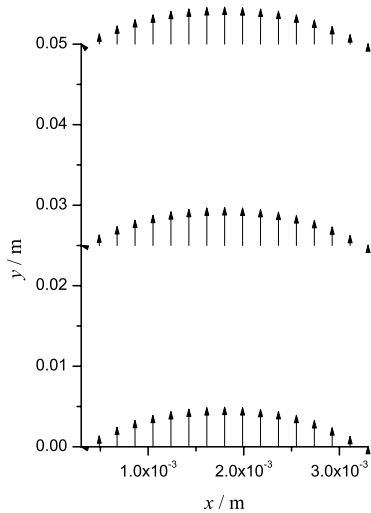
Fig. 6. Model results for velocity field in the gas channel. $T_{cell} = 60$ °C, $j_{ave} = 300$ mA cm^{-2}.

Table 6. Model results for average velocities at the upper end of the channel ($y = L$)

T_{cell} /°C	j_{ave} /mA cm^{-2}	$|\mathbf{u}|_{ave}$ (m s^{-1})
40	100	0.0127
40	200	0.0163
60	100	0.0216
60	200	0.0234
60	300	0.0253

In the boundary condition definitions, it was assumed that the velocity profile at interface between the gas channel and the gas diffusion layer can be approximated using the current distribution at the electrode. The results indicate that the magnitude of average velocity at this boundary is two orders of magnitude lower than the average velocity in the channel. As an example, the average velocity at this boundary was 1.1×10^{-4} m s^{-2} in the $T_{cell} = 60$ °C and $j_{ave} = 300$ mA cm^{-2} case. Therefore, the approximation made in the boundary conditions can be considered justified, because any error at the boundary would also become very small compared to the velocity in the channel.

For comparison, an additional calculation was performed without the 'Darcy-type' term and the 6/5-factor in Equations 4. It was found that without these modifications, the average velocity at the upper end of the channel would be severely overestimated. For example, in the case of $T_{cell} = 60$ °C and $j_{ave} = 300$ mA cm^{-2} the error would be 95%.

The saturation pressure of water vapour increases from 7381.4 to 19932 Pa (an increase of 170%) when temperature is increased from 40 to 60 °C. This, in addition to the effect of flow velocity, explains why flooding problems at the lower temperature level were significantly more severe. As shown in Table 5, water mole fractions of the same magnitude result in a very

Table 7. Effect of varying the net water transport α in the model The operating conditions were $T_{cell} = 60$ °C, $j_{ave} = 300$ mA cm^{-2}. Average velocity is given at $y = L$.

α	Minimum of X_O	Maximum of X_w	$|\mathbf{u}|_{ave}$ /m s^{-1}
−0.4	0.0715	0.0848	0.0222
−0.25	0.0757	0.162	0.0253
−0.1	0.0773	0.225	0.0280

different relative humidity at the different temperature levels.

Because value of the net water transport parameter α was assumed, a set of additional calculations at $T_{cell} = 60$ °C and $j_{ave} = 300$ mA cm^{-2} were performed with different values of α, in order to estimate the magnitude of the uncertainty introduced in the results. The results are given in Table 7 for $α = -0.4$, $α = -0.1$ and the base case $α = -0.25$. Comparison of the results reveals that, despite the large scale of variation in α, the effect on the mole fraction of oxygen is small (6%). The effect on the average velocity is moderate (12%).

4. Discussion

The purpose of this study was to provide theoretical interpretations for current distributions observed in a free-convection cell, and to identify relevant issues for more elaborate modeling work. It was found that in the studied cell type, the removal of water set the limits to performance at the lower temperature level ($T_{cell} = 40$ °C). When the cell temperature was increased to 60 °C, water removal was improved. The model indicates that this resulted partly from increased flow rate and partly from increased saturation pressure of water.

Measured current distributions were used to define boundary conditions for the electrode side of the modelled domain. This allowed us to estimate the oxygen consumption and water production with good precision. A major uncertainty in the present study is the fact that net water transport was assumed. This issue will be elaborated in future work. Despite this uncertainty, it appears very probable that saturation conditions are encountered within the gas diffusion layer and on the electrode surfaces especially at lower temperature. This confirms the importance of developing two-phase models.

Free convection in the channel was modeled using a buoyancy term in the Navier–Stokes equation. The three-dimensional geometry of the channel was accounted for by assuming a Poiseuille profile in the z-direction. A full 3D-model would further improve the accuracy of the model predictions. Furthermore, a 3D-model would enable the calculation of the local conditions under the ribs of the flow field plate.

The model presented here describes a straight-channel geometry with the ends of the channels open to the ambient air. This type of channel geometry is well suited

to a traditional stack structure, which has the benefit of high power density and low internal resistance. In addition to this channel structure, also other types of cell geometries may be feasible for small free-breathing PEMFCs and DMFCs. Examples of designs described in the literature are planar cells [33], annular cells [34, 35], and pseudo-bipolar and strip cell designs [36, 37]. Designs that utilize silicon substrates and related manufacturing techniques may be advantageous in very small systems [2].

Acknowledgements

References

1. A. Heinzel, C. Hebling, M. Müller, M. Zedda and C. Müller, *J. Power Sources* **105** (2002) 250.
2. J.P. Meyers and H.L. Maynard, *J. Power Sources* **109** (2002) 76.
3. C.K. Dyer, *J. Power Sources* **106** (2002) 31.
4. J. Vanhanen, 'On the performance improvements of small-scale photovoltaic-hydrogen systems', Dissertation (Helsinki University of Technology, Espoo, 1996).
5. T.B. Atwater, P.J. Cygan and C.L. Fee, *J. Power Sources* **91** (2000) 27.
6. J.M. Moore, B.J. Lakeman and G.O. Mepsted, *J. Power Sources* **106** (2002) 16.
7. J.W. Raadschelders and T. Jansen, *J. Power Sources* **96** (2001) 160.
8. D. Chu, R. Jiang, K. Gardner, R. Jacobs, J. Schmidt, T. Quakenbush and J. Stephens, *J. Power Sources* **96** (2001) 174.
9. D.M. Bernardi and M. Verbrugge, *AIChE J.* **37** (1991) 1151.
10. D.M. Bernardi and M. Verbrugge, *J. Electrochem. Soc.* **139** (1992) 2477.
11. T.E. Springer, T.A. Zawodzinski and S. Gottesfeld, *J. Electrochem. Soc.* **138** (1991) 2334.
12. T.E. Springer, M.S. Wilson and S. Gottesfeld, *J. Electrochem. Soc.* **140** (1993) 3513.
13. T.F. Fuller and J. Newman, *J. Electrohem. Soc.* **140** (1993) 1218.
14. T.V. Nguyen and R.E. White, *J. Electrochem. Soc.* **140** (1993) 2178.
15. V. Gurau, H. Liu and S. Kakaç, *AIChE J.* **44** (1998) 2410.
16. S. Um, C-Y. Wang and K-S. Chen, *J. Electrochem. Soc.* **147** (2000) 4485.
17. K. Dannenberg, P. Ekdunge and G. Lindbergh, *J. Appl. Electrochem.* **30** (2000) 1377.
18. Z-H. Wang, C-Y. Wang and K-S. Chen, *J. Power Sources* **94** (2001) 40.
19. D. Natarajan and T.V. Nguyen, *J. Electrochem. Soc.* **148** (2001) A1324.
20. W. He, J.S. Yi and T.V. Nguyen, *AIChE J.* **46** (2000) 2053.
21. G.J.M. Janssen, *J. Electrochem. Soc.* **148** (2001) A1313.
22. T. Berning, D.M. Lu and N. Djilali, *J. Power Sources* **106** (2002) 284.
23. A. Rowe and X. Li, *J. Power Sources* **102** (2001) 82.
24. M. Wöhr, K. Bollwin, W. Schnurnberger, M. Fisher, W. Neubrand and G. Eigenberger, *Int. J. Hydrogen Energy* **23** (1998) 213.
25. S. Shimpalee and S. Dutta, *J. Numer. Heat Transf. Part A* **38** (2000) 111.
26. S. Shimpalee, 'Numerical prediction of gas-humidification effects on energy transfer in PEM fuel cells', Dissertation (University of South Carolina, Columbia, 2001).
27. M. Noponen, T. Mennola, M. Mikkola, T. Hottinen and P. Lund, *J. Power Sources* **106** (2002) 304.
28. M. Noponen, T. Hottinen, T. Mennola, M. Mikkola and P. Lund, *J. Appl. Electrochem.*, submitted and accepted.
29. M. Roos, U. Harnisch and T. Hocker, 'Incompressible Flow Through Ducts', Internal report (Center for Computational Physics, Zürich University of Applied Sciences Winterthur, Switzerland, 2002).
30. K-T. Lee, *Int. J. Heat Mass Transf.* **42** (1999) 4523.
31. E.N. Fuller, P.D. Schettler and J.C. Giddings, *Ind. Eng. Chem.* **58** (1966) 19.
32. R.B. Bird, W.E. Stewart and E.N. Lightfoot, 'Transport phenomena'. (J. Wiley & Sons, New York, 1960).
33. J. Neutzler, J.W. Bostaph and A.M. Fisher, *Patent WO 0 249 136* (2002).
34. M.S. Wilson, *US Patent 5 514 486* (1996).
35. J.K. Neutzler and M.S. Wilson, *US Patent 5 595 834* (1997).
36. R. Jiang and D. Chu, *J. Power Sources* **93** (2001) 25.
37. H. Chang, J-R. Kim, J-H. Cho, H-K. Kim and K-H. Choi, *Solid State Ionics* **148** (2002) 601.